LAWRENCE
LIVERMORE
NATIONAL
LABORATORY

LLNL-JRNL-666489

Metal/ceramic interface structures and segregation behavior in aluminum-based composites

X. Zhang, T. Hu, J. F. Rufner, T. LaGrange, G. H. Campbell, E. J. Lavernia, J. M. Schoenung, K. van Benthem

January 23, 2015

Acta Materialia

Disclaimer

This document was prepared as an account of work sponsored by an agency of the United States government. Neither the United States government nor Lawrence Livermore National Security, LLC, nor any of their employees makes any warranty, expressed or implied, or assumes any legal liability or responsibility for the accuracy, completeness, or usefulness of any information, apparatus, product, or process disclosed, or represents that its use would not infringe privately owned rights. Reference herein to any specific commercial product, process, or service by trade name, trademark, manufacturer, or otherwise does not necessarily constitute or imply its endorsement, recommendation, or favoring by the United States government or Lawrence Livermore National Security, LLC. The views and opinions of authors expressed herein do not necessarily state or reflect those of the United States government or Lawrence Livermore National Security, LLC, and shall not be used for advertising or product endorsement purposes.

Metal/ceramic interface structures and segregation behavior in aluminum-based composites

Xinming Zhang[1], Tao Hu[1], Jorgen F. Rufner[1], Thomas LaGrange[2*], Geoffrey H. Campbell[2],

Enrique J. Lavernia[1], Julie M. Schoenung[1], Klaus van Benthem[1]

[1]*Department of Chemical Engineering and Materials Science, University of California, Davis, CA 95616*

[2]*Physical and Life Sciences Directory, Lawrence Livermore National Laboratory, 7000 East Ave, Livermore, CA 94550*

Abstract

Trimodal Al alloy (AA) matrix composites consisting of ultrafine-grained (UFG) and coarse-grained (CG) Al phases and micron-sized B_4C ceramic reinforcement particles exhibit combinations of strength and ductility that render them useful for potential applications in the aerospace, defense and automotive industries. Tailoring of microstructures with specific mechanical properties requires a detailed understanding of interfacial structures to enable strong interface bonding between ceramic reinforcement and metal matrix, and thereby allow for effective load transfer. Trimodal AA metal matrix composites typically show three characteristics that are noteworthy: nanocrystalline grains in the vicinity of the B_4C reinforcement particles; Mg segregation at AA/B_4C interfaces; and the presence of amorphous interfacial layers separating nanocrystalline grains from B_4C particles. Interestingly, however, fundamental information related to the mechanisms responsible for these characteristics as well as information on local compositions and phases are absent in the current literature. In this study, we use high-resolution transmission electron microscopy, energy-dispersive X-ray

[*] Now at: Integrated Dynamic Electron Solutions, Inc.

spectroscopy, electron energy-loss spectroscopy, and precession assisted electron diffraction to gain fundamental insight into the mechanisms that affect the characteristics of AA/B_4C interfaces. Specifically, we determined interfacial structures, local composition and spatial distribution of the interfacial constituents. Near atomic resolution characterization revealed amorphous multilayers and a nanocrystalline region between Al phase and B_4C reinforcement particles. The amorphous multilayers consist of nonstoichiometric Al_xO_y, while the nanocrystalline region is comprised of MgO nanograins. The experimental results are discussed in terms of the possible underlying mechanisms at AA/B_4C interfaces.

1. Introduction

Nanostructured (<100nm) and ultrafine-grained (100-500nm) materials are noteworthy because they provide an opportunity to study the influence of microstructural dimensions on mechanical behavior. Remarkable enhancements to mechanical strength and physical performance have been documented for such materials [1–4]. One strategy to produce nanostructured or UFG materials involves severe plastic deformation (SPD) using, for instance, equal channel angular pressing, high pressure torsion [5], surface mechanical attrition treatment [6], and ball milling [2,7]. A derivative of ball milling that has been broadly used to prepare nanocrystalline microstructures is cryogenic ball milling (cryomilling), which takes advantage of cryogenic temperatures to suppress dynamic recrystallization by dissipating heat generated during the milling process [2]. Regardless of the synthesis technique, room temperature ductility and strain hardening of nanocrystalline materials are genrally degraded by the limited dislocation activity that occurs at these grain sizes [8–11]. A number of

approaches, such as the introduction of coarse grains, precipitate particles and promoting twin formation, have been successfully used to enhance the ductility of nanocrystalline materials[12]. Another approach involves the development of trimodal metal matrix composites, which consist of a coarse grained (CG) structure (larger than 1 µm grain size), an ultrafine-grained (UFG) structure, and micron-sized B_4C reinforcement particles [13–16]. The CG structure is employed to provide ductility, while the UFG structure facilitates grain boundary strengthening due to, e.g., the Hall-Petch relationship. The B_4C particles pin the movement of dislocations to further resist plastic deformation, lower the material's density and increase the elastic modulus of the metal matrix composite.

Inspection of the published literature shows that the mechanical behavior of trimodal composites has been studied for the past decade [13–15,17,18]. A widely used matrix is Al-Mg partly due to the excellent balance of strength, weldability and corrosion resistance of this family of alloys [19]. The original trimodal composite [14], consisting of 10 wt.% micron-sized B_4C, 40 wt.% UFG 5083 AA and 50 wt.% CG 5083 AA, was manufactured through cryomilling, blending, cold isostatic pressing and extrusion. This composite exhibited ultra-high compression yield strength of 1065 MPa. Early trimodal composites established themselves as attractive alternatives to conventional armor steel due to their excellent dynamic deformation behavior, with strain-to-failure of 14% at strain rates on the order of 10^3 s^{-1} and strength values as high as 1000 MPa [13,20]. However, widespread application of the early trimodal composites was restrained by their limited strain-to-failure (0.8%) when tested under quasi-static compression, and failure prior to yielding when tested under tensile loading.

Modifications of the trimodal composite with a higher content of the CG phase led to tensile yielding but with limited elongation (1-2%) [15]. More recently, Zhang et al. [21] showed that nanometric B_4C reinforcement suppressed stress/strain localization and thereby improved plasticity. In this particular study a trimodal composite consisting of 3.5 wt.% nano-sized B_4C, 30 wt.% CG 5083 AA and the balance UFG 5083 AA was reported to exhibit a strength above 630 MPa with a tensile strain of 3% [21].

A critical requirement for the application of trimodal composites is the creation of a strong interfacial bond between ceramic reinforcement and metal matrix to allow for effective load transfer. To that effect, the interfacial structures that form between Al and B_4C reinforcements in 5083 AA trimodal composite have been studied using high resolution transmission electron microscopy (HRTEM) [8,17,22]. Li et al. [17,22] reported the presence of amorphous layers, with a typical thickness between 5-8 nm, separating B_4C particles and the UFG Al phase. The authors suggested that the interfacial layers likely originated from the native surface oxide of 5083 AA during processing [17], but detailed studies were not conducted to ascertain the origin of these layers. Hence, the possibilities that the interface layers originated from either amorphization of crystalline B_4C [23] under shock load or from amorphous boron oxide [24] due to surface oxidation were not considered.

The formation of one to three layers of nanocrystalline grains with diameters of approximately 30-50 nm at the Al/B_4C interface has also been reported previously [8,22]. Segregation of Mg to Al/B_4C interfaces was demonstrated using electron energy loss spectroscopy (EELS) and energy-dispersive X-ray spectroscopy (EDXS) [17,25]. Vogt et al.

suggested that nucleation of micro-cracks approximately 100 nm away from the AA/B_4C interfaces may have led to failure during compression testing [13]. However, studies of interfacial phenomena focused on only small length fractions of grain boundaries and did not provide a global understanding of the characteristics and possible influence of interfacial composition and structure. For example, no energy-loss near-edge fine structure (ELNES) studies have been performed to provide bonding information for the elements segregated to the interface. Hence, information on the relationship between different interface morphologies (e.g., amorphous layers, nanocrystalline grains, etc.) and their chemical composition profiles remains absent in the literature.

In view of the above discussion, we determine microstructure information from HRTEM, EDXS, EELS, and precession assisted electron diffraction. The experimental results are used to ascertain a fundamental insight into the mechanisms that affect the characteristics of Al/B_4C interfaces.

2. Experimental details

2.1. Materials synthesis

The feedstock powders used to produce trimodal Al matrix composites were gas-atomized 5083 AA (4.5 wt.% Mg, 0.57 wt.% Mn, 0.25 wt.% Fe balanced with Al) provided by Valimet, Inc. (Stockton, CA) and B_4C powder (Tetrabor©, F1200) from ESK Ceramics (Saline, MI). The as-received 5083 AA powder had an average particle size below 45 µm. The particle size for the as-received B_4C powder ranged from 1-7 µm [26]. The composite powder was fabricated via cryomilling [2] of 14 wt.% B_4C and 76 wt.% UFG 5083 AA for 24 hours using stainless steel balls

as grinding media. Chemical analysis of the cryomilled powder was completed by Luvak, Inc. (Boylston, MA) and Shiva Technologies (Syracuse, NY). Non-metallic elements were measured using combustion infrared detection and inert gas fusion, while metallic elements were measured using direct current plasma emission spectroscopy. The chemical composition analysis of the as-cryomilled powder before mixing with CG 5083 AA is shown in Table 1 [26]. After cryomilling the powder was mixed with CG 5083 AA.

The mixed powder consisting of three different components was compacted to approximately 50% relative density inside a nitrogen glove box and subsequently degassed in a furnace to remove hydrogen and oxygen introduced by the surfactant (stearic acid) used during milling. Degassing was performed at $4x10^{-5}$ Torr while the sample was heated over 4 hours up to 400°C with a holding time of 8 hours. Degassing was considered completed when the pressure reached $2x10^{-6}$ Torr. Degassed powders were subsequently consolidated by hot isostatic pressing (HIP) at 400 ± 4°C and 101.3 ± 1.7 MPa for 4 hours. Extrusion was used for secondary consolidation at a rate of 48.8 m/min. To aid with the deformation during extrusion, the billets were pre-heated in a furnace at 525°C for 30 minutes and then extruded at a ratio of 6.5:1. The final product is designed to consist of 10 wt.% B_4C, 30 wt.% CG 5083 AA, and the balance of UFG 5083 AA [25]. The grain sizes of these microconstituents after consolidation were determined through TEM to be 400-600 nm, 600-2600 nm, and 174 ± 100 nm, respectively. More detailed information about the synthesis procedure is published elsewhere [14,18,25,26].

Table 1 Chemical analysis of cryomilled powder after milling for 24 hrs.

O (wt. %)	H (ppm)	N (wt. %)	Fe (wt. %)	Mn (wt. %)
12.64	1263	3.10	0.47	0.57

2.2. Microstructure Characterization

The morphology and structure of different phases and their interfaces was investigated by transmission electron microscopy (TEM) using either a JEOL JEM-2500SE instrument (JEOL Ltd., Tokyo, Japan) at University of California, Davis (UCD), or a FEI monochromated F20 UT Tecnai scanning transmission electron microscope (FEI Company, Hillsboro, OR) at the National Center for Electron Microscopy (NCEM). Scanning transmission electron microscopy (STEM) was carried out with a Titan G2 80-200 instrument (FEI Company, Hillsboro, OR) equipped with ChemiSTEM technology and a Fischione high angle angular dark field (HAADF) detector (Fischione, Export, PA) at the FEI Nanoport (Hillsboro, OR). All microscopes were operated at 200 kV.

Electron-transparent TEM samples were prepared with either a FEI Versa 3D focused ion beam (FIB) at the FEI Nanoport, or a FEI Scios FIB at UCD. The starting voltage was 30 kV for trenching and initial thinning. The accelerating voltage of the ion beam was then reduced to 5 kV when sample thickness reached approximately 400 nm. Final thinning was performed at 2 kV when the TEM lamellae became electron-transparent. After final thinning, an ion beam energy of 0.5 kV was used to remove most of the remaining amorphous damage layers from the sample surfaces. The final thickness of the TEM samples was approximately 60 nm.

2.3. Chemical Composition Characterization

Elemental distribution maps were acquired using an FEI Super-X windowless EDXS detector (FEI Company, Hillsboro, OR) installed on the Titan G2 80-200 instrument described above. EELS line scans and energy-loss near-edge fine structures (ELNES) were recorded with a Gatan Tridiem parallel electron energy loss spectrometer attached to the aberration corrected JEOL JEM 2100F/Cs scanning transmission electron microscope at UCD, or the monochromated F20 UT Tecnai instrument at NCEM. All microscopes were operated at 200 kV.

Multivariate statistical analysis (HREM Research Inc., Japan) was used to reduce random noise from as-acquired EELS data using principle component analysis. The software decomposes acquired spectrum images into eigenspectra with assigned eigenvalues. EELS spectra were subsequently reconstructed by using only statistically relevant principal constituents [27,28].

2.4. Precession Assisted Electron Diffraction

Precession assisted electron diffraction (PED) was used to study the crystalline orientation of the Al matrix near the Al/B_4C interface. The advantage of PED over electron back-scattered diffraction is that the achievable spatial resolution is determined by the diameter of the converged electron beam rather than by the detector-specimen geometry during SEM. Detailed information regarding the specifics and underlying physics of this technique are reported elsewhere [29–32]. PED was performed using a Phillips CM300 transmission electron microscope (FEI Company, Hillsboro, OR) equipped with the NanoMEGAS Digistar hardware controlled by the Topspin™ precession control platform (AppFive LLC, Arizona) at Lawrence Livermore National Laboratory. The microscope was operated at 300 kV.

3. Results

3.1. Microstructure identification

Fig. 1a shows a typical TEM bright field image of the 5083 AA trimodal composite in which the B_4C, UFG Al and CG Al regions are labeled. The dashed curve marks the interface between a CG region and an UFG region. The UFG regions generally show darker contrast when compared to CG regions due to the fact that smaller grain size allows for stochastically oriented grains, and, hence, variations in dynamical diffracting conditions. B_4C particles reveal a faceted morphology and are mostly distributed throughout the UFG regions. The observed distribution of B_4C particles is caused by their addition to UFG regions during cryomilling, which leads to limited contact with CG regions that were introduced after cryomilling [22]. Fig. 1b shows a SEM micrograph at lower magnification that provides more detailed information about the distribution of CG Al, UFG Al and B_4C particles within the 5083 AA trimodal composite. SEM characterization reveals the B_4C particles with relative dark contrast and confirms that they are embedded in UFG regions. CG regions exhibit no B_4C particles over large areas of the microstructure. Fig. 1b also demonstrates that B_4C particles are distributed within the UFG regions that are clearly separated from the CG regions. The high aspect ratio of CG and UFG regions is a result of the extrusion process with a direction indicated by the arrow in Fig. 1b.

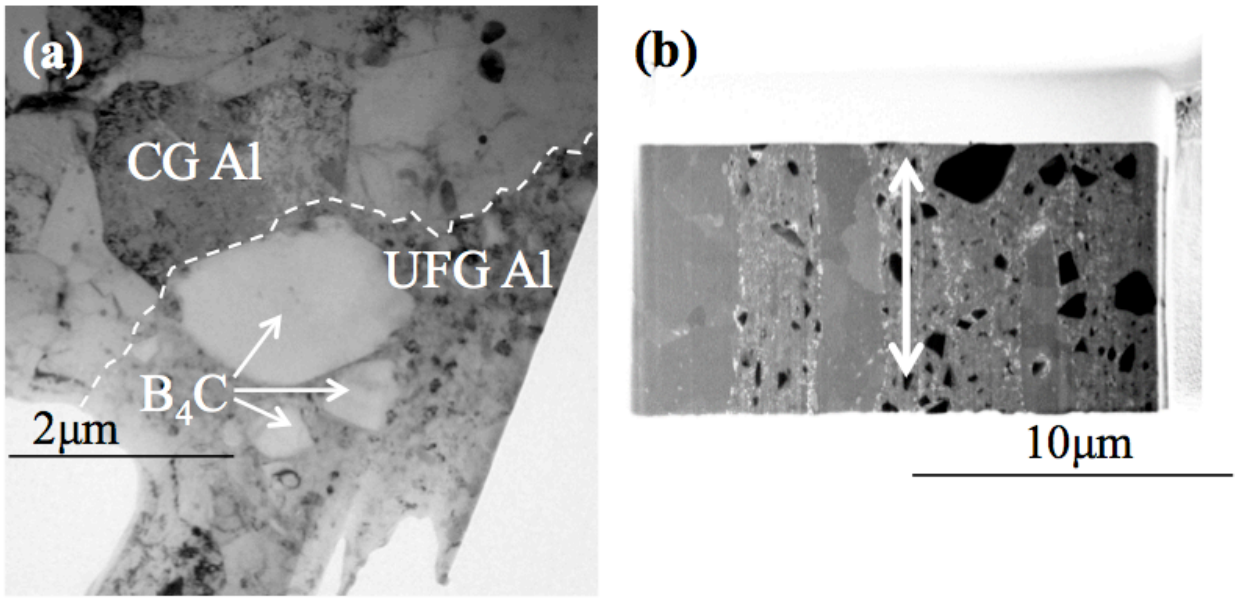

Fig. 1 (a) TEM image showing micro constituents of CG, UFG and B_4C within 5083 AA trimodal composite; (b) SEM imaging of a TEM sample prepared by FIB showing the distribution of CG, UFG and B_4C particles within 5083 AA trimodal composite. The extrusion direction is marked by the white arrow.

3.2. Interface composition and structures

Fig. 2a shows a B_4C particle in contact with CG Al on one side (Interface 1) and UFG Al at interfaces 2-4. Local chemical compositions and segregation behavior at interfaces were determined by EDXS analysis. The resulting elemental distribution maps for Mg, Al, B, C, Fe are shown in Fig. 2b-g, respectively. The distribution of Mn directly correlates with that of Fe. Fig. 2b demonstrates prominent segregation of Mg at Interface 1 between B_4C and CG Al; such segregation of Mg also exists for interfaces between B_4C and UFG Al (Interfaces 2 and 3) with weaker signal and a more diffuse contrast for Mg. For Interface 4 there is no obvious sign of Mg segregation. Other interfaces surrounding smaller B_4C grains in Fig. 2 show similar trends for Mg segregation. The elemental map in Fig. 2c shows a homogeneous distribution of Al, while Mg-rich layers observed in Fig. 2b appear depleted in Al. The elemental distribution maps for B

and C in Figs. 2d and 2e, respectively, confirm the identity of the large B_4C grain. Distributions of Fe and Mn are shown in Fig. 2f and 2g reveal that Fe and Mn are confined to small dispersoids randomly distributed throughout the microstructure. Fig. 3 shows elemental distribution maps for Al, Mg, B, and C obtained from EDXS data acquired at higher magnification from the marked area of Interface 1 (see Fig. 2a). The elemental maps confirm the presence of a layered interface structure with Al signals (Fig. 3a) recorded from the area between the B_4C particle and the Mg-rich layer (Fig. 3b). Quantitative EDXS analysis reveals an Al/O atomic ratio equal to 1.47 ± 0.29 from this Al-rich region. Consistent with Fig. 2 the location of the B_4C particle is identified from B (Fig. 3c) and C signals (Fig. 3d). Fig. 3d reveals the presence of carbon within the Al-rich layer adjacent to the B_4C particle.

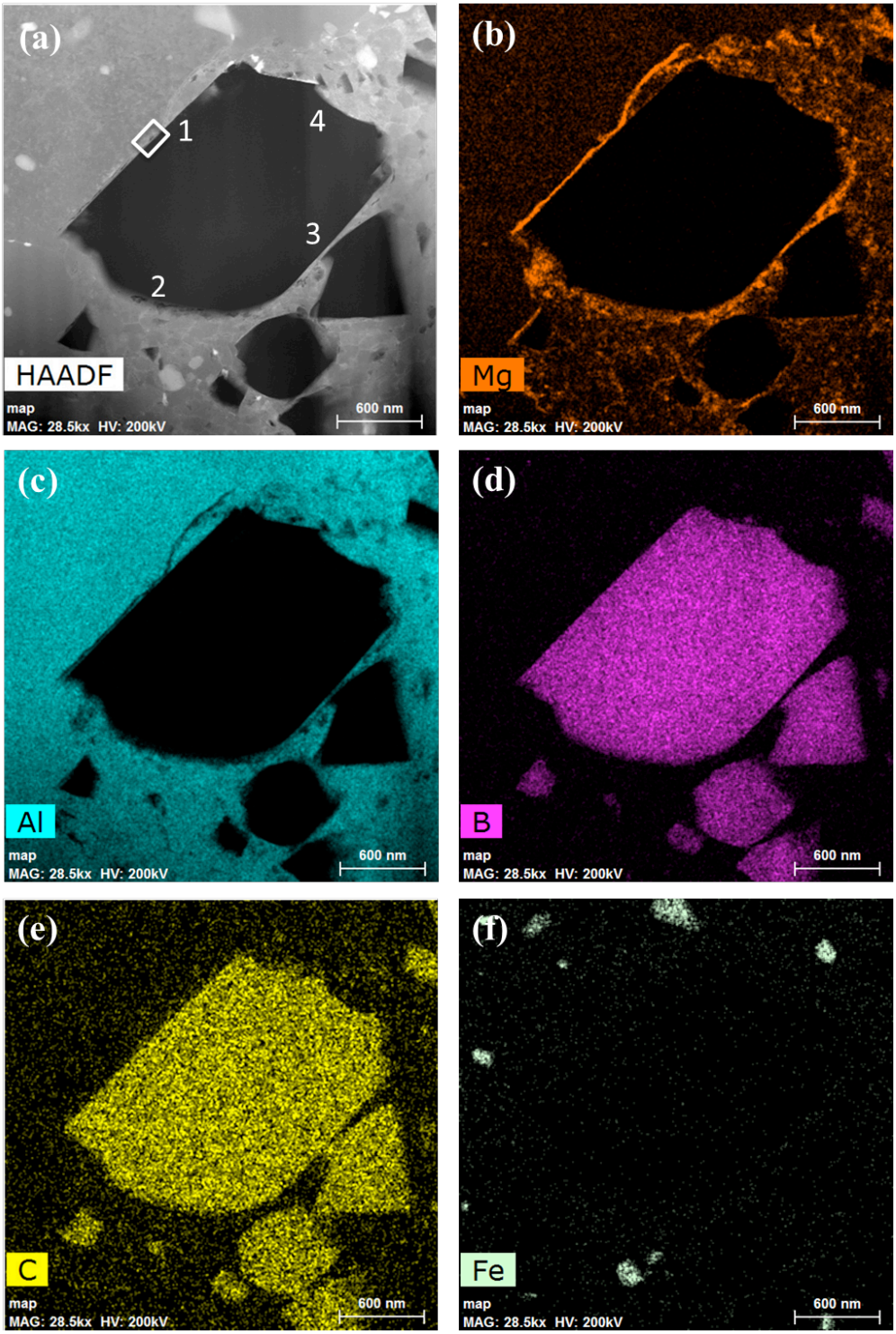
(a)
1
2
3
4
HAADF
map
MAG: 28.5kx HV: 200kV
600 nm
(b)
Mg
map
MAG: 28.5kx HV: 200kV
600 nm
(c)
Al
map
MAG: 28.5kx HV: 200kV
600 nm
(d)
B
map
MAG: 28.5kx HV: 200kV
600 nm
(e)
C
map
MAG: 28.5kx HV: 200kV
600 nm
(f)
Fe
map
MAG: 28.5kx HV: 200kV
600 nm

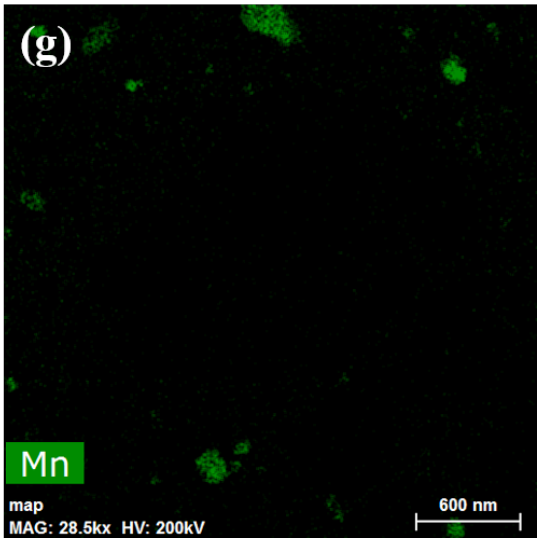

Fig.2 (a) High-angle annular dark field STEM image showing a B_4C particle located in the center of the image that is in contact with both a CG Al region at Interface 1 and UFG Al regions at Interfaces 2-4; EDXS maps illustrate the distribution of (b) Mg, (c) Al, (d) B, (e) C, and (f) Fe within the trimodal composite.

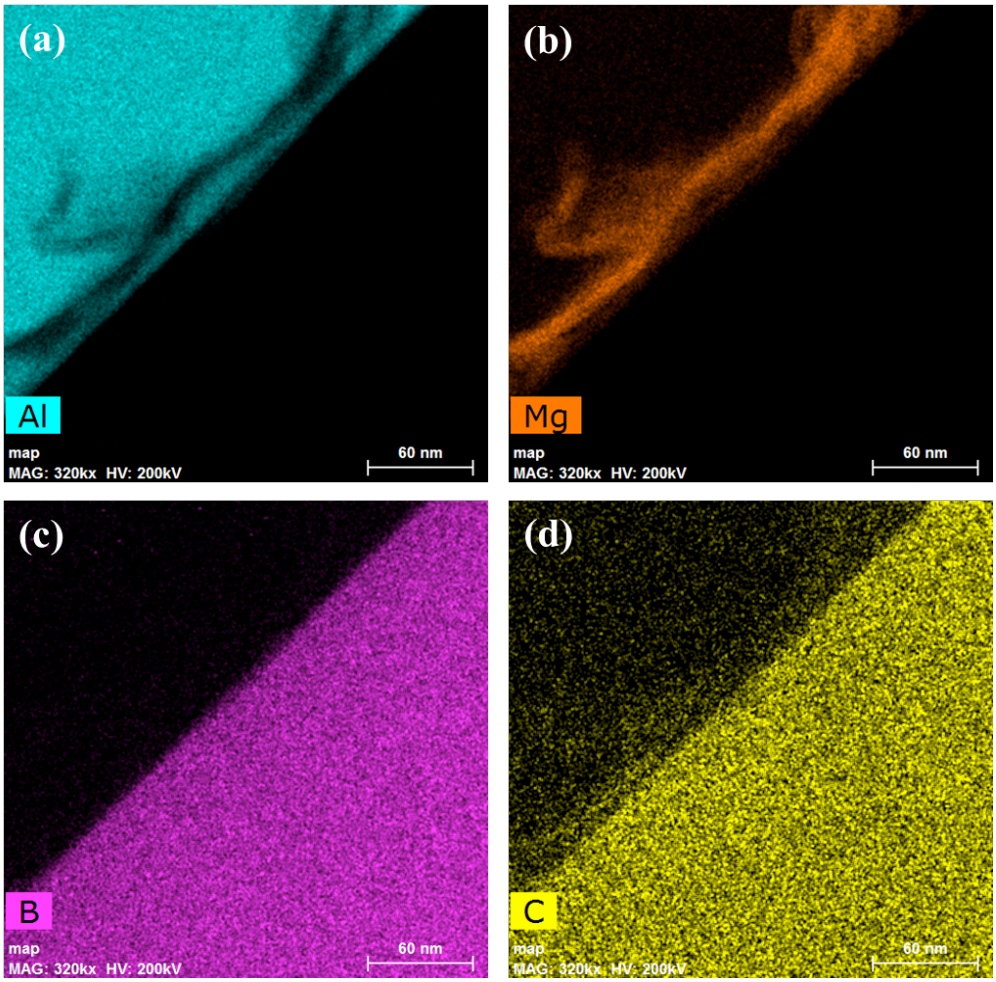

Fig.3 EDXS maps illustrating the distribution of: (a) Al, (b) Mg, (c) B and (d) C within the framed area of Fig. 2(a).

For a more detailed analysis of the interface morphologies, diffraction contrast bright field TEM images were recorded from all areas around the central B_4C grain in Fig. 2. Fig. 4 shows a composite micrograph in which the individual TEM images were merged through maximizing the cross-correlation functions of the respective image overlap regions. The locations of Interfaces 1 through 4 are marked in the inset in the center of Fig. 4. Interface 1 reveals the contact between CG Al and the B_4C particle. A significant number of areas with dark contrast are observed in the CG region indicating the presence of dislocations. The arrow in Fig. 4 marks

a site where the Mg segregation layer transitions from a straight line to a curved morphology (cf. Fig. 2b). The straight dashed line is the CG Al/B_4C interface, while the dashed curve marks an interface between the CG and UFG regions. The Mg-rich layer shows uniform thickness and accommodates the shape of the CG Al. Interfaces 2 and 4 are curved UFG Al/B_4C interfaces, while Interface 3 is a straight UFG Al/B_4C interface that is parallel to Interface 1. A brief summary of morphologies and structures of Interfaces 1 through 4 is listed in Table 2.

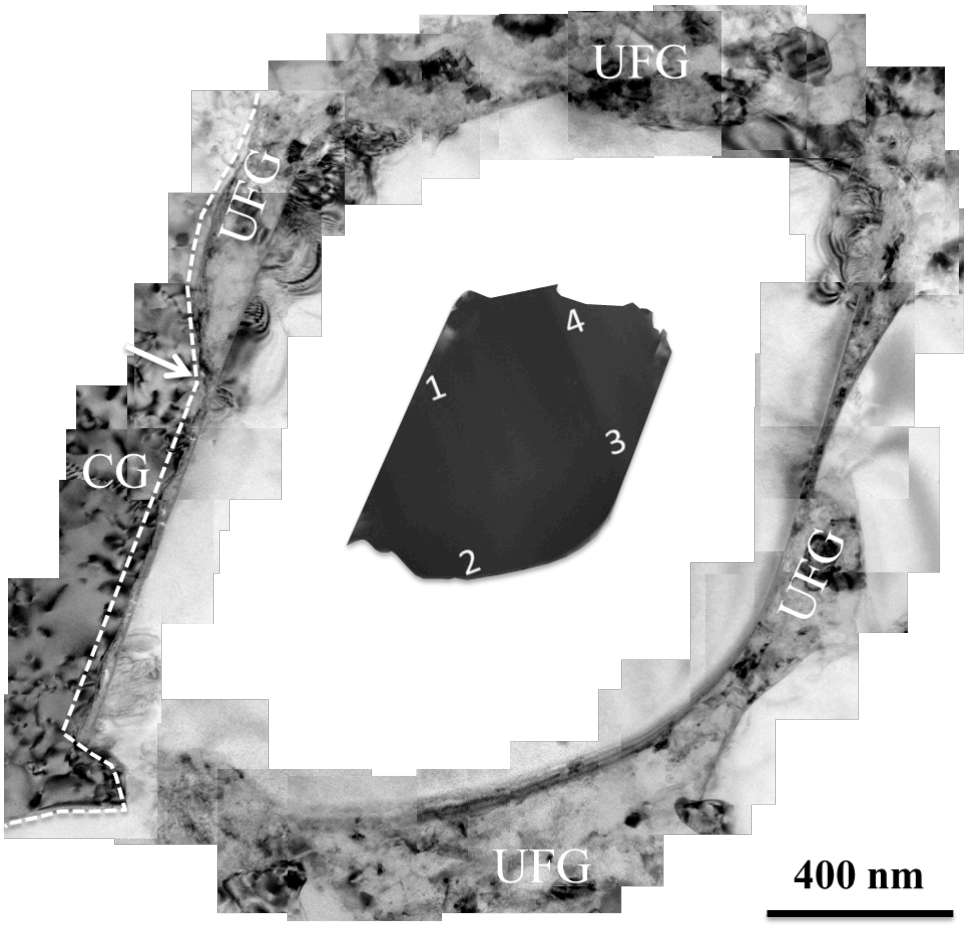

Fig.4 Collage of TEM bright field images showing the different interfacial structures noted in Fig. 2, with the dashed line indicating the boundary of the CG Al region.

Table 2. Summary of interfacial morphologies and structures.

	Interface 1	Interface 2	Interface 3	Interface 4
Morphology	Straight	Curved	Curved	Curved
Configuration	UFG/B_4C (top), CG/B_4C (bottom)	UFG/B_4C	UFG/B_4C	UFG/B_4C
Mg segregation	Strong	Weak, diffuse	Weak, diffuse	None

The structure and morphology of the double-layered structure between B_4C and CG Al (cf. Fig. 2 and 3) was further investigated by HRTEM. Micrographs recorded at medium resolution (Fig. 5a) and the HRTEM micrograph in Fig. 5b both show significant variations in layer thickness. The width of the interface varies between 20 and 25 nm. Fig. 5c shows that the Mg-rich layer is polycrystalline. Different grains are outlined with dashed markings. The thickness of the Mg-rich layer is approximately 18 ± 4 nm. Measurements of lattice spacing from several different grains are consistent with those for MgO (e.g., $d_{(200)}$=2.01 ± 0.01 Å in Fig. 5c and $d_{(111)}$= 2.31 ± 0.05 Å in Fig. 5d) [33]. As shown in Fig. 5c and 5d, the HRTEM contrast suggests the presence of an additional amorphous region between the Mg segregation layer and the B_4C particle. That amorphous layer's (marked by dashed markings) thickness varies between 2 and 6 nm. The observation of this amorphous layer is consistent with previous studies on trimodal Al systems [8,17,22].

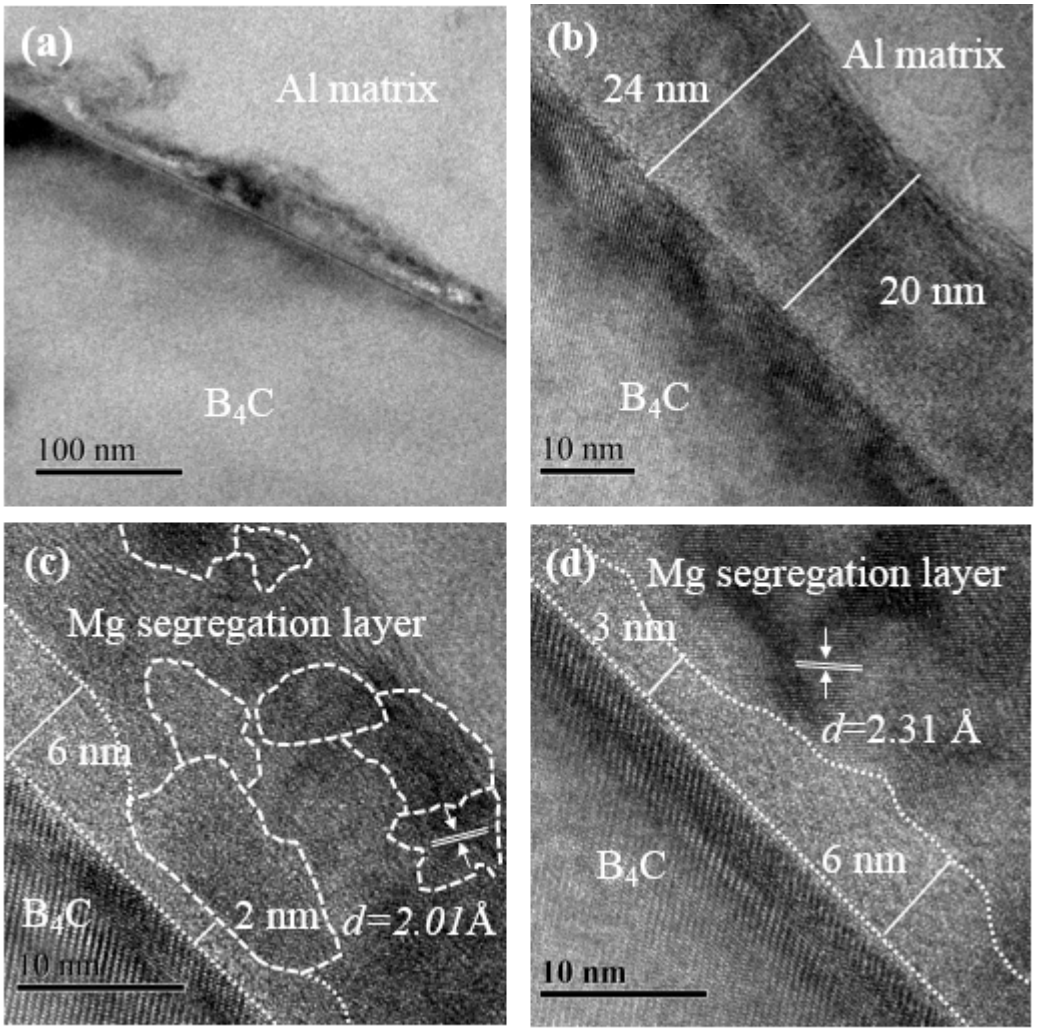

Fig.5 (a) Bright field TEM image of the interface between the B_4C particle and the Al matrix; (b) TEM image revealing the thickness of the Mg-rich layer; (c) HRTEM image showing a double-layered interface consists of amorphous layer and polycrystalline Mg-rich layer, the lattice spacing of the Mg-rich layer is measured to be 2.01± 0.01 Å for (200) planes and 2.31± 0.05 Å for (111) planes; (d) TEM image revealing the existence of an amorphous layer between the B_4C and the Mg-rich layer with a thickness of 3-6 nm.

For a more detailed analysis of the local chemical composition, EELS intensity line profiles were recorded across Interfaces 1 and 2. Fig. 6a shows the integrated EELS intensity across the CG Al/B_4C interface (Interface 1) as a function of relative distance. In the direction

from the CG Al to B_4C particle, the Al K-edge EELS intensity drops significantly to a minimal value at a relative distance of approximately 13 nm and shows a local maximum value of approximately 24 nm, the position of later Al peak coincides with that of the amorphous layer observed in Fig. 5. The signal extracted from the Mg K-edge, however, peaks at approximately 12.5 nm with a significantly wider full width at half maximum (FHWM) compared to that of the Al signal. In between the CG Al and B_4C phases, two peaks for the integrated O K-edge intensity are observed and coincide with the locations of the peaks observed for Mg and Al, respectively. The EELS intensity profiles reproduce the EDXS data presented in Fig. 3. Chemical composition profiling therefore suggests that the amorphous layer is an oxide rich in Al, while the nanocrystalline layer is a Mg-rich oxide.

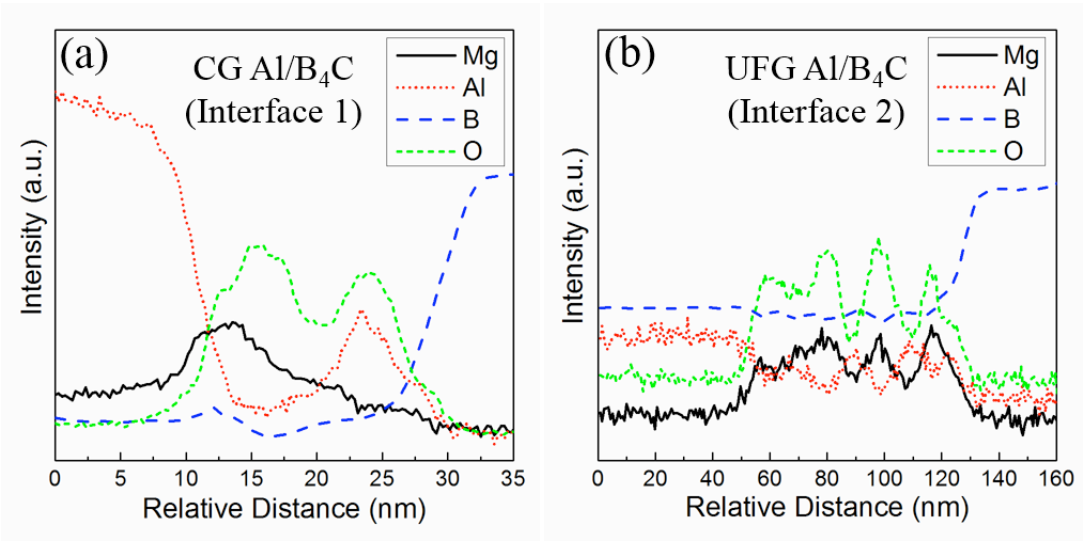

Fig. 6 Integrated EELS intensity as a function of position obtained from: (a) CG Al/B_4C Interface 1and (b) UFG Al/B_4C Interface 2, showing signals for Mg, Al, B and O.

Fig. 6b shows the integrated EELS intensity profiles for the UFG Al/B_4C interface (Interface 2). Between the UFG metal Al matrix and the B_4C particle, multiple peaks of for Mg and Al

intensities are observed. Where the Mg peak is at a maximum, the Al peak is at a minimum, and vice versa. The O signal reveals maximum intensities coinciding with the Mg signal only. However, the oxygen maximum intensity closest to the B_4C grain reveals a shoulder at a relative distance of 125 nm, which coincides with a maximum in the Al signal for the location where the Al matrix is in direct contact with the B_4C particle. This observation is consistent with the EDXS results presented above (Fig. 3a and b) and confirms the existence of an Al-rich oxide layer between the Mg-rich phase and B_4C for the UFG Al/B_4C interface (Interface 2). Over extended distances, UFG Al/B_4C interfaces reveal multiple layers of nanocrystalline magnesium oxide between the metal matrix and the reinforcing particle.

The HRTEM micrograph in Fig. 7a was recorded from Interface 4 where UFG Al is in direct contact with B_4C with no amorphous layer present. The corresponding EELS intensity line profiles in Fig. 7b reveal no Mg and O EELS intensities for this interface configuration.

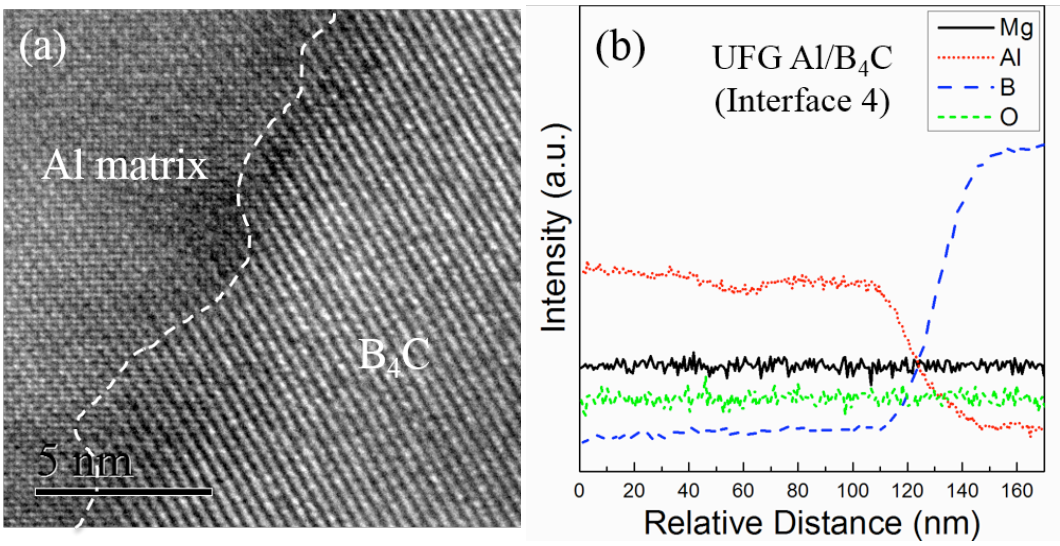

Fig. 7 (a) TEM image revealing a direct contact between the UFG Al and the B_4C (Interface 4) with the dashed curve highlighting the interface. (b) Integrated EELS intensity as a function of position obtained from Interface 4 showing

signals for Mg, Al, B and O.

The local bonding environment at the CG Al/B_4C interface was investigated through ELNES of the O K-edge. Fig. 8a and 8b show the as-acquired O K-edge ELNES obtained from the Mg-rich layer and from the amorphous layer adjacent to the B_4C particle, respectively. The experimental spectra are compared to reference spectra for Al_2O_3 and MgO [34]. The experimental ELNES data show agreement with the respective reference data and confirm that the amorphous layer adjacent to the B_4C particle consists of Al oxide (Al_xO_y) and the Mg-rich layer is comprised of MgO. Fig. 8c shows the spatially resolved B K and C K ELNES recorded from the B_4C particle interior, the B_4C/Al_xO_y interface, and the amorphous Al_xO_y layer (cf. Fig. 5). The spectra reveal no boron or carbon signals from the amorphous layer, while the EELS intensities at the B_4C/Al_xO_y interface are significantly lower compared to the bulk B_4C spectrum.

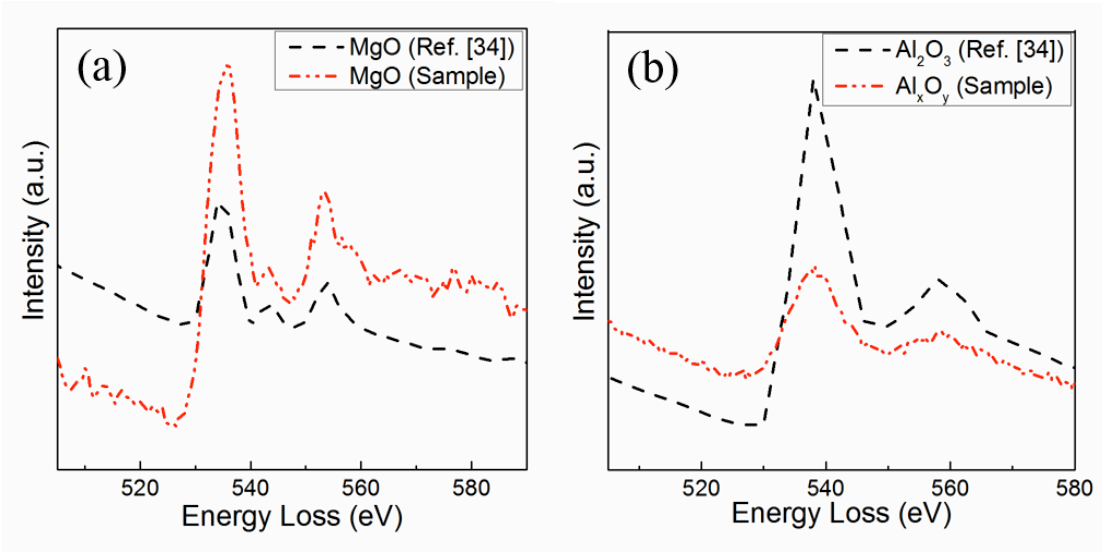

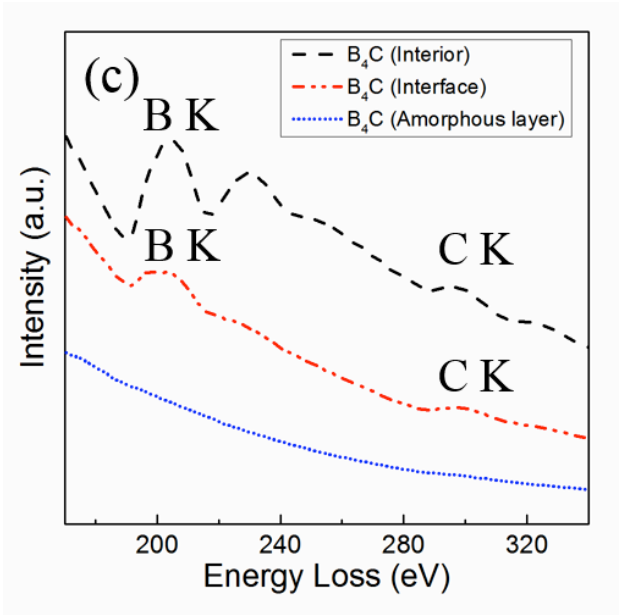

Fig. 8 (a) ELNES spectra showing Mg K-edge for MgO obtained from the Mg-rich layer and the MgO standard. (b) Al K-edge obtained from the amorphous layer compared to a reference spectrum for bulk Al_2O_3 [34]. (c) B K- and C K-ELNES recorded from the interior of the B_4C particle, the B_4C/Al_xO_y interface, and the interior of the amorphous Al_xO_y layer.

3.3 Crystalline orientation near interface

PED mapping was performed for the UFG Al/B_4C interface (Interface 2) to evaluate whether the interface morphology may correlate with any texturing in the UFG area. Fig. 8a shows an HAADF STEM image of the same area discussed above, with an orientation map extracted from the PED analysis overlaid on the STEM image. Diffraction signals recorded from the B_4C particle and the MgO layer were removed from the results for ease of analysis and better presentation. The color-coded orientation map reveals no preferred orientation of the grains in the UFG

region with respect to the B_4C particle. For a more detailed analysis, <001>, <110> and <111> pole figures of the area mapped in Fig. 9a are plotted in Fig. 9b and show no dominant texture of the metallic matrix in the vicinity of the B_4C particle.

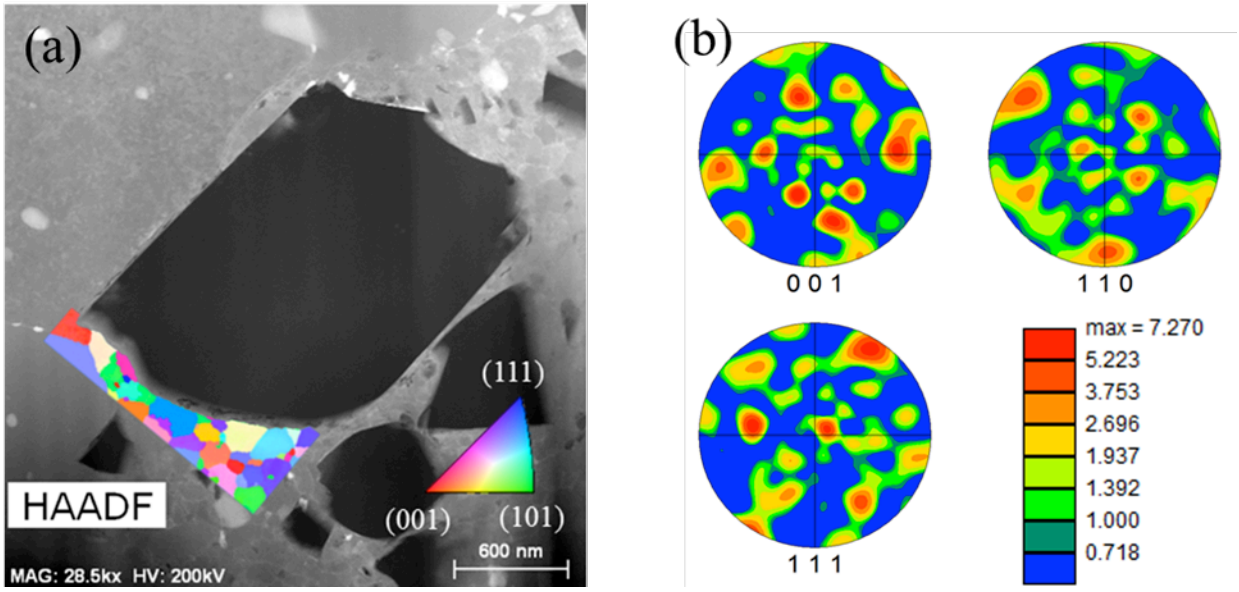

Fig. 9 (a) Distribution of grain orientations in the UFG 5083 AA adjacent to Interface 2. (b) [001], [110], [111] pole figures showing the texture of PED data shown in (a).

4. Discussion

4.1 Interfacial structure and composition

The experimental results obtained in this study reveal a 2-6 nm thick amorphous layer with Al_xO_y composition surrounding the B_4C particles, and the presence of one or multiple polycrystalline MgO layer(s) separating the amorphous layer from the CG or UFG metal matrix, respectively. Quantitative EDXS analysis reveals such amorphous aluminum oxide layers are non-stoichiometric and enriched with Al (Al/O= 1.47 ± 0.29 atomic ratio) that is consistent with work from Jeurgens et al. [34]. It was previously assumed that the amorphous layer originates

from surface oxidization of 5083 AA during processing and handling of the 5083 AA powder [36]. However, crystalline B_4C may undergo amorphization under high strain rate deformation, as it was shown under shock loading in ballistic tests [23], or during nanoindentation [37]. Cryomilling may have similar impact and could lead to the formation of the observed amorphous layer discussed above. The C K-ELNES is sensitive to detect amorphous B_4C by the presence of a π^* excitation at the edge onset [23,37,38]. Fig. 8c demonstrates that neither the B K-edge nor the C K-edge were detected from the amorphous layer and there was no significant change in the C K-edge ELNES line shape at the interface between the amorphous oxide layer and B_4C. Hence, no electrons have been excited to an unoccupied π^* level. The ELNES analysis therefore confirms the predicted surface oxidization of aluminum rather than amorphization of boron carbide.

The combination of HRTEM imaging and chemical composition profiling revealed that each Mg-rich layer is comprised of polycrystalline MgO with a thickness of approximately 20 nm (Fig. 6). This result suggests that the previously observed nanocrystalline layers between B_4C and the UFG Al matrix [8,22] are of MgO composition rather than nanocrystalline Al grains. This conclusion was derived from the following three observations: firstly, the location of the Mg-rich grains between the B_4C reinforcement and the UFG Al matrix is identical that of what was previously described as nanocrystalline Al grains; secondly, the size of the Mg-rich grains (approximately 20 nm) is consistent with the size of what was previously described as nanocrystalline Al grains, which is finer than the size of the UFGs that result after cryomilling plus thermo-mechanical consolidation; thirdly, typically 2-4 layers of nanocrystalline Al grains

had been reported to be present between the B_4C particles and the UFG Al matrix, which agrees with the EELS observations of four layers of Mg-rich grains, as shown in Fig. 6b.

The amorphous Al_xO_y layer, although not directly observed at the UFG Al/B_4C interface due to the projection view in TEM experiments, always separates the nanocrystalline MgO from the B_4C grains (see EELS profiles in Fig. 6). Therefore, MgO is never in direct contact with the B_4C reinforcements.

4.2 Amorphous Al_xO_y and nanocrystalline MgO

The oxidation of metallic aluminum and the formation of native oxide surface layers is almost unavoidable during processing as the standard formation enthalpy for Al_2O_3 is -1675.7 kJ/mol [39]. An unrealistic oxygen partial pressure at or below 10^{-143} Torr is required to avoid oxidization of clean Al [40]. Hence, the oxidation products in the trimodal composite can be traced to four possible sources. First, the feedstock metal powders utilized for this study typically contain surface oxide layers, which stabilize the powders during atomization [40]. Second, during cryomilling, the powder particles are continuously fragmented and new clean Al surfaces are created. A turbulent mixing process during cryomilling was adopted for our experiments to allow boiling N_2 to escape, but this also introduces oxygen that leads to oxidization of the newly created clean Al surfaces. Third, whereas the as-cryomilled powder is stored in a glove box maintained under an argon atmosphere, the prevalent oxygen partial pressure is also sufficient to allow for further oxidization of clean Al powder surfaces. Fourth, another source for the observed Al_xO_y is the reaction of Al with water vapor that is generated

during the degassing process. [26,41]. Water vapor originates from chemisorbed water on prior Al_xO_y surfaces, and from physisorbed water on the Al powder surface.

Amorphous Al_xO_y layers have the potential to crystallize to γ-Al_2O_3 at elevated temperatures [35,42]. However, no crystalline Al_2O_3 was observed in the trimodal microstructures investigated in this study. The transition from amorphous to crystalline aluminum oxide is debated in the literature. For oxide film thickness below 4 nm the amorphous phase is commonly sub-stoichiometric in oxygen (Al_xO_y) and is thermodynamically more stable than the crystalline state (Al_2O_3) [35,42]. However, no universal agreement exists on the critical thickness for the structural transition, which is dependent on multiple parameters, including the crystalline orientation of the Al surface, the partial pressure of oxygen, the particle size of Al, and temperature [43–45]. Crystalline transitions into Al_2O_3 require growth of native amorphous Al_xO_y to reach both a critical thickness and correct stoichiometry in the presence of oxygen and elevated temperatures [35]. During this study both conditions are only satisfied during the degassing process with limited oxygen concentrations from the decomposition of water vapor and surfactants left after cryomilling. Thus, with limited oxygen available during the degassing process and oxygen from Al_xO_y being continuously consumed to form MgO, it is more likely for Al_xO_y to grow non-stoichiometrically and maintain an amorphous structure. The observed presence of carbon within the Al_xO_y layer (cf. Fig. 3d) is due to the remaining free carbon that originates from surfactants added during cryomilling [26].

The experimental results reveal Mg segregation to the surface of the Al grains and the formation of nanocrystalline MgO between the metal matrix grains and the amorphous oxide

layer. The standard formation enthalpy for MgO is -601.6 kJ/mol [39]. Hence, MgO is thermodynamically more stable than Al_2O_3. Mg atoms present inside the Al grains near the surface will locally consume oxygen from the amorphous Al_xO_y to form MgO. This mechanism causes a depletion of metallic Mg in surface regions within the metal matrix and thus creates a driving force for segregation of Mg towards the grain surfaces. Fig. 10 shows a schematic diagram of Mg segregation that leads to the formation of the observed nanocrystalline MgO interface layer. Previous studies have shown that such diffusion of Mg can lead to the formation of MgO, $MgAl_2O_4$ or a mixture of the two on the surface of the aluminum alloy [46,47]. However, the ELNES results in Fig. 8 show no sign of any spectral features that are characteristic for the $MgAl_2O_4$ spinel structure [48]. Formation of $MgAl_2O_4$ requires additional oxygen compared to the formation of MgO and can therefore be neglected.

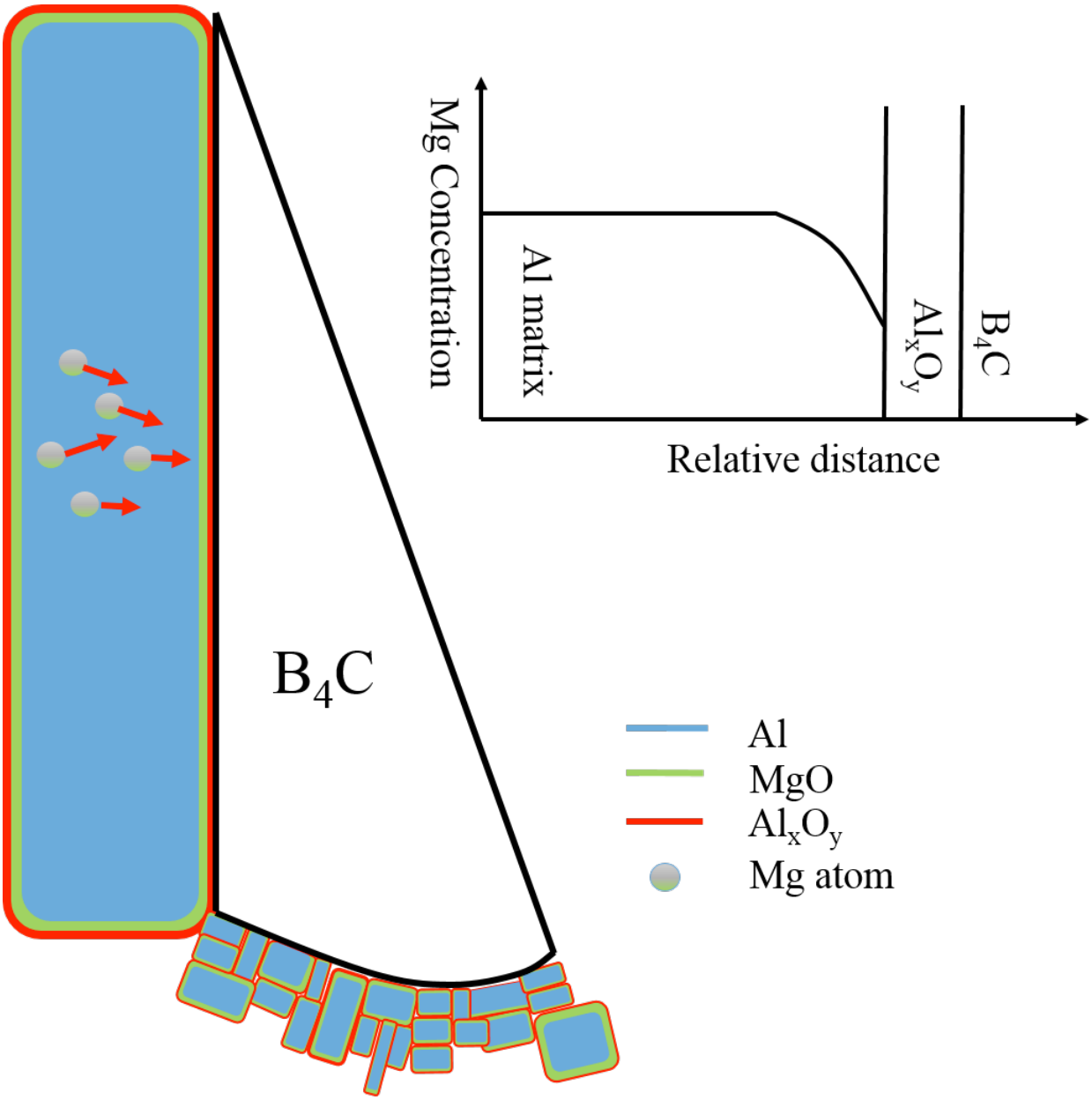

Fig. 10 Schematic diagram showing formation of nanocrystalline MgO and amorphous Al_xO_y layers around the B_4C reinforcement.

PED shows that there is no dominant texture in the Al matrix near the Mg-rich layer. It is therefore concluded that the formation of MgO is independent of the orientation and surface energy of the Al grains. Fig. 2b and Fig. 4 show that the polycrystalline layer of MgO

accommodates the shape of the CG region at Interface 1(with UFG region separating the MgO layer from the B_4C particle). From this observation it is concluded that the segregation behavior for Mg and subsequent formation of MgO is directly related to the presence of amorphous Al_2O_3 on the surface of CG Al and is not affected by the crystal orientation of B_4C particles. This interpretation is consistent with the observation that no Mg segregation is observed in the absence of any surface aluminum oxides (cf. Fig. 7).

The interfaces between CG Al regions and B_4C particles exhibit a single layer of MgO while UFG Al/B_4C interfaces reveal multiple layers of MgO. This is due to the fact that UFG Al regions have more grain boundary area that not only provides more Al_2O_3 interface area but also more diffusion pathways for the formation of MgO (cf. Fig. 10).

4.3 Interfacial properties

Metal/ceramic interfaces in metal matrix composites such as Al/B_4C are often characterized by relatively weak bonding between the different constituents [49]. The absence of pores or voids from the Al/B_4C interfaces could be attributed to the wetting behavior of amorphous aluminum oxide at the ceramic particle surfaces. In contrast, a direct contact between crystalline Al grains and B_4C particles would cause lattice mismatches at the metal/ceramic interface and, hence, an increase in the interface energy [22,50].

In related work, Vogt et al. observed cracks in the metal matrix that formed 100-200 nm away from the Al/B_4C interfaces in 5083 AA trimodal composites during compression tests [13]. The size of the MgO grains of approximately 20-25 nm, and the presence of multiple MgO layers between the UFG Al region and the B_4C reinforcement particles is consistent with the

distance between the observed location for crack initiation and the surface of the B_4C particles. More detailed investigations, including *in-situ* TEM experiments, are required to determine whether the interface strength between the nanocrystalline MgO and the UFG Al matrix is considerably smaller than that between the other constituents in this trimodal system.

5. Conclusions

Two different interfacial structures have been observed at Al/B_4C interfaces in 5083 AA trimodal composites: existence of an amorphous layer with a thickness ranging between 2 and 6 nm, and the existence of nanocrystalline grains smaller in size than the grains in the bulk UFG Al regions). EDXS and EELS studies demonstrate that the amorphous layer consists of aluminum oxide, and that amorphous layer separates the B_4C reinforcement particle from one or multiple layer(s) of nanocrystalline MgO. The formation of MgO grains is due to the fact that Mg has a higher affinity for O than Al and diffuses toward the Al_2O_3 surface layer. No evidence was found for a correlation of the formation of MgO with the orientation of the Al matrix or the B_4C reinforcement particles. The experimental results suggest that the presence of both amorphous aluminum oxide and at least one layer of nanocrystalline MgO improve the interfacial bonding and wetting capability of the Al/B_4C interfaces.

6. Acknowledgements

X.Z., J.F.R. and K.v.B. were financially supported by a University of California Laboratory Fee grant (#12-LR-238313). J.M.S., T.H. and E.J.L received funding from the Office of Naval Research (program manager: Dr. Lawrence Kabacoff) under grant number N00014-12-1-0237. The FIB instrument at UC Davis was acquired with grant number N00014-13-1-0668 from Office of

Naval Research (program manager: Dr. Lawrence Kabacoff). The precession electron diffraction experiments were performed under the auspices of the U.S. Department of Energy, Office of Basic Energy Sciences, Division of Materials Sciences and Engineering at Lawrence Livermore National Laboratory under Contract DE-AC52-07NA27344 and supported by FWP SCW0974 with equipment capabilities established under FWP SCW0939. We acknowledge support from the National Center for Electron Microscopy, Lawrence Berkeley National Lab, which is supported by the US Department of Energy under contract no. DE-AC02-05CH11231.

References

[1] H. Hahn, K.A. Padmanabhan, Mechanical response of nanostructured materials, Nanostructured Mater. 6 (1995) 191-200.

[2] D.B. Witkin, E.J. Lavernia, Synthesis and mechanical behavior of nanostructured materials via cryomilling, Prog Mater Sci. 51 (2006) 1-60.

[3] P. Moriarty, Nanostructured materials, Rep Prog Phys. 64 (2001) 297-381.

[4] C.C. Koch, The synthesis and structure of nanocrystalline materials produced by mechanical attrition: A review, Nanostructured Mater. 2 (1993) 109-129.

[5] R. Valiev, R. Islamgaliev, I. Alexandrov, Bulk nanostructured materials from severe plastic deformation, Prog Mater Sci. 45 (2000) 103-189.

[6] K. Lu, J. Lu, Nanostructured surface layer on metallic materials induced by surface mechanical attrition treatment, Mater Sci Eng A. 375-377 (2004) 38-45.

[7] G. Lucadamo, N.Y.C Yang, C.S. Marchi, E.J. Lavernia, Microstructure characterization in cryomilled Al 5083, Mater Sci Eng A. 430 (2006) 230-241.

[8] B. Yao, C. Hofmeister, T. Patterson, Y. Sohn, M. van den. Bergh M, T. Delahanty, K. Cho, Microstructural features influencing the strength of Trimodal Aluminum Metal-Matrix-Composites, Compos Part Appl Sci Manuf. 41 (2010) 933-941.

[9] E. Ma, Instabilities and ductility of nanocrystalline and ultrafine-grained metals, Scr Mater. 49 (2003) 663-668.

[10] Legros, B. R. Elliott, M. N. Rittne M, Microsample tensile testing of nanocrystalline metals, Philos Mag A. 80 (2000) 1017-1026.

[11] B.O. Han, E.J. Lavernia, Z. Lee, S. Nutt, D. Witkin, Deformation behavior of bimodal nanostructured 5083 Al alloys, Metall Mater Trans A. 36 (2005) 957-965.

[12] Y. Zhao, Y. Zhu, E.J. Lavernia, Strategies for improving tensile ductility of bulk nanostructured materials, Adv Eng Mater. 12 (2010) 769-778.

[13] R.G. Vogt, Z. Zhang, E. Huskins, B. Ahn, S. Nutt, K.T. Ramesh, E.J. Lavernia, J.M. Schoenung, High strain rate deformation and resultant damage mechanisms in ultrafine-grained aluminum matrix composites, Mater Sci Eng A. 527 (2010) 5990-5996.

[14] J. Ye, B.Q. Han, Z. Lee, B. Ahn, S.R. Nutt, J.M. Schoenung, A tri-modal aluminum based composite with super-high strength, Scr Mater. 53 (2005) 481-486.

[15] J. Ye, B.Q. Han, J.M. Schoenung, Mechanical behaviour of an Al–matrix composite reinforced with nanocrystalline Al-coated B_4C particulates, Philos Mag Lett. 86 (2006) 721-732.

[16] J. Ye, J. He, J.M. Schoenung, Cryomilling for the fabrication of a particulate B4C reinforced Al nanocomposite: Part I. Effects of process conditions on structure, Metall Mater Trans A. 37 (2006) 3099-3109.

[17] Y. Li, Z. Zhang, R. Vogt, J.M. Schoenung, E.J. Lavernia, Boundaries and interfaces in ultrafine grain composites, Acta Mater. 59 (2011) 7206-7218.

[18] R.G. Vogt, Z. Zhang, T.D. Topping, E.J. Lavernia, J.M. Schoenung, Cryomilled aluminum alloy and boron carbide nano-composite plate, J Mater Process Technol. 209 (2009) 5046-5053.

[19] M.A. Meyers, Mechanical Behavior of Materials, 2nd ed. Cambridge University Press, New York, 2009.

[20] H. Zhang, J. Ye, S.P. Joshi, J.M. Schoenung, E.S.C. Chin, G.A. Gazonas, K.T. Ramesh, Superlightweight nanoengineered aluminum for strength under impact, Adv Eng Mater. 9 (2007) 355-359.

[21] Z. Zhang, T. Topping, Y. Li, R. Vogt, Y. Zhou, C. Haines, J. Paras, D. Kapoor, J.M. Schoenung, E.J. Lavernia, Mechanical behavior of ultrafine-grained Al composites reinforced with B_4C nanoparticles, Scr Mater. 65 (2011) 652-655.

[22] Y. Li, Y.H. Zhao, V. Ortalan, W. Liu, Z.H. Zhang, R.G. Vogt, N.D Browning, E.J. Lavernia, J.M. Schoenung, Investigation of aluminum-based nanocomposites with ultra-high strength, Mater Sci Eng A. 527 (2009) 305-316.

[23] M. Chen, Shock-induced localized amorphization in boron carbide, Science. 299 (2003) 1563-1566.

[24] S.J. Hwang, C. Fernandez, J.P. Amoureux, J. Cho, S.W. Martin, M. Pruski, Quantitative study of the short range order in B_2O_3 and B_2S_3 by MAS and two-dimensional triple-quantum MAS 11B NMR, Solid State Nucl. Magn. Reson. 8 (1997) 109-121.

[25] Y. Li, W. Liu, V. Ortalan, W.F. Li, Z. Zhang, R. Vogt, N.D. Browning, E.J. Lavernia, J.M. Schoenung, HRTEM and EELS study of aluminum nitride in nanostructured Al 5083/B_4C processed via cryomilling, Acta Mater. 58 (2010) 1732-1740.

[26] R. Vogt. Ultrafine-grained aluminm and boron carbide metal matrix composites. [S.l.]: Proquest, Umi Dissertatio; 2011.

[27] M. Watanabe, E. Okunishi, K. Ishizuka, Analysis of spectrum-imaging datasets in atomic-resolution electron microscopy, Microsc Anal. 2009 5-7.

[28] C-H. Chang, J.F. Rufner, K van. Benthem, R.H.R Castro, Design of desintering in tin dioxide Nanoparticles, Chem Mater, 25 (2013) 4262-4268.

[29] R. Vincent, P.A. Midgley, Double conical beam-rocking system for measurement of integrated electron diffraction intensities, Ultramicroscopy. 53 (1994) 271-282.

[30] J.G. Brons, G.B. Thompson, Orientation mapping via precession-enhanced electron diffraction and its applications in materials science, JOM. 66 (2014) 165-170.

[31] A. Avilov, K. Kuligin, S. Nicolopoulos, M. Nickolskiy, K. Boulahya, J. Portillo, G. Lepeshov, B. Sobolev, J.P. Collette, N. Martin, A.C. Robins, P. Fischione, Precession technique and electron diffractometry as new tools for crystal structure analysis and chemical bonding determination, Ultramicroscopy. 107 (2007) 431-444.

[32] J. Gjønnes, V. Hansen, A. Kverneland, The precession technique in electron diffraction and its application to structure determination of nano-size precipitates in alloys, Microsc Microanal. 10 (2004) 16-20.

[33] 2014 International Centre for Diffraction Data-04-006-5939. n.d.

[34] Gatan EELS Atlas. Gatan Inc 2010.

[35] L.P.H. Jeurgens, W.G. Sloof, F.D. Tichelaar, E.J. Mittemeijer, Composition and chemical state of the ions of aluminium-oxide films formed by thermal oxidation of aluminium, Surf Sci. 506 (2002) 313-332.

[36] Y-W Kim, W.M. Griffith, F.H. Froes, Surface oxides in P/M aluminum alloys, JOM. 37 (1985) 27-33.

[37] D. Ge, V. Domnich, T. Juliano, E. Stach, Y. Gogotsi, Structural damage in boron carbide under contact loading, Acta Mater. 52 (2004) 3921-3927.

[38] V. Domnich, S. Reynaud, R.A. Haber, M. Chhowalla, Boron carbide: structure, properties, and stability under stress, J Am Ceram Soc. 94 (2011) 3605-3628.

[39] J. Cox, D. Wagman, V. Medvedev, CODATA Key Values for Thermodynamics, Hemisphere Pub. Corp., New York, 1989.

[40] L. Kowalski, B.M. Korevaar, J. Duszczyk, Some new aspects of the theory of oxidation and degassing of aluminium-based alloy powders, J Mater Sci. 27 (1992) 2770-2780.

[41] Z. Zhang, S. Dallek, R. Vogt, Y. Li, T.D. Topping, Y. Zhou, J.M. Schoenung, E.J. Lavernia, Degassing behavior of nanostructured Al and its composites, Metall Mater Trans A. 41 (2010) 532-541.

[42] L.P.H. Jeurgens, W.G. Sloof, F.D. Tichelaar, E.J. Mittemeijer, Structure and morphology of aluminium-oxide films formed by thermal oxidation of aluminium, Thin Solid Films. 418 (2002) 89-101.

[43] M.A. Trunov, M. Schoenitz, X. Zhu, E.L. Dreizin, Effect of polymorphic phase transformations in Al2O3 film on oxidation kinetics of aluminum powders, Combust Flame. 140 (2005) 310-318.

[44] J.C. Sánchez-López, A.R. González-Elipe, A. Fernández, Passivation of nanocrystalline Al prepared by the gas phase condensation method: An x-ray photoelectron spectroscopy study, J Mater Res. 13 (1998) 703-710.

[45] L.P.H. Jeurgens, W.G. Sloof, F.D. Tichelaar, E.J. Mittemeijer, Growth kinetics and mechanisms of aluminum-oxide films formed by thermal oxidation of aluminum, J Appl Phys. 92 (2002) 1649-1656.

[46] P. Krizik, M. Balog, E. Illekova, P. Svec, I. Matko, M. Stepanek, M. Nosko, F.J. Simancik, The oxidation behavior of gas-atomized Al and Al alloy powder green compacts during heating before hot extrusion and the suggested heating process, Mater Process Technol. 214 (2014) 1165-1172.

[47] G.R. Wakefield, R.M. Sharp, The composition of oxides formed on Al-Mg alloys, Appl Surf Sci. 51 (1991) 95-102.

[48] K. Van Benthem, H. Kohl, Methods for ELNES-quantification: characterization of the degree of inversion of Mg–Al-spinels, Micron. 31 (2000) 347-354.

[49] T.W. Clyne, An Introduction to Metal Matrix Composites. Cambridge University Press, New York, 1993.

[50] R. Benedictus, A. Böttger, E. Mittemeijer, Thermodynamic model for solid-state amorphization in binary systems at interfaces and grain boundaries, Phys Rev B. 54 (1996) 9109-9125.

Figure Captions

Table 1 Chemical analysis of cryomilled powder sampled at milling time of 24 hrs.

Table 2 Summary of interfacial morphologies and structures.

Fig. 1 (a) TEM image showing micro constituents of CG, UFG and B_4C within trimodal system. (b) SEM imaging of a TEM sample prepared by TEM showing the distribution of CG, UFG and B_4C particles within MMC extrusion direction is marked with white arrow.

Fig.2 (a) High-angle annular dark field STEM image showing a B_4C particle located in the center of the image that is in contact with both a CG Al region at Interface 1 and UFG Al regions at Interfaces 2-4; EDXS maps illustrate the distribution of (b) Mg, (c) Al, (d) B, (e) C, and (f) Fewithin the trimodal composite.

Fig.3 EDXS mapping works showing distribution of (a)Al, (b)Mg, (c)B and (d)C within the framed area of Fig. 2(a).

Fig.4 TEM image showing different interfacial structures involved in Fig. 2 with the dash line marks the position of CG.

Fig.5 (a) Bright field TEM image of the interface between the B_4C particle and the Al matrix; (b) TEM image revealing the thickness of the Mg-rich layer; (c) HRTEM image showing a double-layered interface consists of amorphous layer and polycrystalline Mg-rich layer, the lattice spacing of the Mg-rich layer is measured to be 2.01± 0.01 Å for (200) planes and 2.31± 0.05 Å for (111) planes; (d) TEM image revealing the existence of an amorphous layer between the B_4C and the Mg-rich layer with a thickness of 3-6 nm.

Fig.6 Integrated EELS intensity as a function of position obtained from: (a) CG Al/B_4C Interface 1and (b) UFG Al/B_4C Interface 2, showing signals for Mg, Al, B and O.

Fig. 7 (a) TEM image revealing a direct contact between the UFG Al and the B_4C (Interface 4) with the dashed curve highlighting the interface. (b) Integrated EELS intensity as a function of position obtained from Interface 4 showing signals for Mg, Al, B and O.

Fig.8 (a) ELNES spectra showing Mg K-edge for MgO obtained from the Mg-rich layer and the MgO standard. (b) Al K-edge obtained from the amorphous layer compared to a reference spectrum for bulk Al_2O_3 [34]. (c) B K- and C K-ELNES recorded from the interior of the B_4C particle, the B_4C/Al_xO_y interface, and the interior of the amorphous Al_xO_y layer.

Fig. 9 (a) PED mapping overlaid with HAADF image at UFG 5083 AA/B_4C interface. (b) [001], [110], [111] pole figures showing the texture of PED data shown in (a).

Fig. 10 Schematic showing formation of MgO around B_4C reinforcement.